Real-time Monitoring of Urinary Stone Status During Shockwave Lithotripsy

Peter A. Noble

OBJECTIVE To develop a standardized, real-time feedback system for monitoring urinary stone fragmentation during shockwave lithotripsy (SWL), thereby optimizing treatment efficacy and minimizing patient risk.

METHODS A 2-pronged approach was implemented to quantify stone fragmentation in C-arm X-ray images. First, the initial pre-treatment stone image was compared to subsequent images to measure stone area loss. Second, a Convolutional Neural Network was trained to estimate the probability that an image contains a urinary stone. These 2 criteria were integrated to create a real-time signaling system capable of evaluating shockwave efficacy during SWL.

RESULTS The system was developed using data from 522 shockwave treatments encompassing 4057 C-arm X-ray images. The combined area-loss metric and Convolutional Neural Network output enabled consistent real-time assessment of stone fragmentation, providing actionable feedback to guide SWL in diverse clinical contexts.

CONCLUSION The proposed system offers a novel and reliable method for monitoring urinary stone fragmentation during SWL. By helping to balance treatment efficacy with patient safety, it holds significant promise for semi-automated SWL platforms, particularly in resource-limited or remote environments such as arid regions and extended space missions. UROLOGY xx: xxx–xxx, xxxx.

Urinary stones can cause intense pain by obstructing urine flow and irritating the urinary tract lining, potentially leading to bleeding, infection, or other complications if left untreated. Shockwave lithotripsy (SWL) uses high-energy shockwaves to fragment stones into smaller pieces (< 4 mm) that can pass naturally.[1,2] During treatment, patients typically undergo 5-25 shockwave applications, each generating shockwaves and a corresponding C-arm X-ray image. A fluoroscopy machine, featuring a C-shaped arm that connects the X-ray source to the detector, enables real-time dynamic imaging of internal structures during SWL and produces the X-ray images.

Determining the optimal point to stop SWL treatment is challenging. SWL operators generally follow a predefined protocol, delivering approximately 2000-3000 shockwaves per session, depending on factors such as stone size, composition, location, and the patient's condition. Delivering insufficient shockwaves may leave stones inadequately fragmented to pass out the body, while excessive shockwaves risk tissue damage and complications such as hematoma. Variations in stone size, composition, and location further complicate fragmentation assessment. Stones are initially visible in imaging, but as they fragment, smaller pieces disperse into a cloud and blend into the background,[3] reducing visibility in C-arm images.[4] Current imaging systems cannot reliably determine when fragmentation is complete,[5,6] making it difficult to stop treatment based on visual cues. No reliable metric exists to compare initial and fragmented stone areas after each application. A system that quantifies stone area changes and provides real-time feedback to operators could improve treatment efficiency and reduce complications while balancing fragmentation goals with patient safety.

Artificial intelligence (AI) is transforming medicine by enhancing diagnostics, personalizing treatment, and improving patient outcomes through advanced data analysis and pattern recognition. AI utilizes artificial neural networks, including Convolutional Neural Networks (CNNs), designed to analyze images and perform tasks such as object recognition. CNNs could be used to distinguish urinary stones in X-ray images from other structures, such as bones. These models learn from data, enabling predictions without explicit task-specific programming. In urology, AI has been used to predict lithotripsy outcomes,[7,8] detect kidney stones in videos[9]

From the Department of Microbiology, University of Alabama Birmingham, Birmingham, AL

Address correspondence to: Peter A. Noble, Ph.D., Department of Microbiology, University of Alabama Birmingham, 845 19th Street South, Birmingham, AL 35294. E-mail: panoble@uab.edu

Submitted: May 1, 2025, accepted (with revisions): July 17, 2025

https://doi.org/10.1016/j.urology.2025.07.044
0090-4295

and images,[10-15] predict sepsis risk,[16,17] and optimize lithotripsy outcomes[18-20] and SWL machine parameters.[21]

The objective of the study was to develop an approach that provides real-time status updates on urinary stones during SWL based on thousands of stone images collected during treatments. The approach compares the initial stone area with its current area after each shockwave application, calculates the probability that the object in the image is a stone, and uses a signaling system to notify the operator of the stone's status. To our knowledge, this is one of the first signaling systems developed for monitoring urinary stone fragmentation during SWL.

MATERIALS AND METHODS

Ethics Statement

The research relied on the analysis of anonymized X-ray data accessed through the publicly available "Kidney Stone Registry" (https://bit.ly/4cQSIIZ). The Kidney Stone Registry is a global clinical database that provides anonymized patient information (eg, age, Body Mass Index), treatment parameters (settings used to fragment stones), and X-ray images of SWL and laser ureteroscopy treatments. The purpose of the database is to provide data to medical researchers so they can determine best practices and trends through analytics and statistical analysis with the long-term goal of improving patient outcomes and experiences. The dataset lacked identifiable information, ensuring no possible linkage to personal data. The study was conducted as a retrospective analysis of anonymized records, in accordance with standard ethical guidelines for secondary use of clinical data.

Electronic Medical Data

The C-arm X-ray dataset consisted of 11,648 images, along with information on stone location and size, collected from patients who underwent SWL at multiple sites across the United States between April 21, 2022, and May 5, 2022. The images were generated using various shockwave instruments, including the Dornier Compact Delta II and III, Dornier Compact Sigma, Storz F2, and Storz SLX-T, all operated by experienced physicians/operators.

Software Development

The software developed in this study was run on a MacBook Pro with an Apple M2 Max chip, 32 GB of memory, and the macOS Sequoia 15.1.1 platform. The following libraries were utilized: OpenCV, OpenMP, and Standard C++.

Stone Probability Calculator

A stone image dataset was created using a custom-designed program, which draws a 50 × 50 pixel green box around a stone and exports the cropped stone image to an external folder after the user clicks on a stone in the image (Supplementary Fig. 1). An initial screening of the X-ray images yielded 4621 stone images and 4621 non-stone images. Further curation to remove ambiguous images resulted in a final dataset of 2804 stone images and 2804 non-stone images (examples are shown in Supplementary Fig. 2).

Preprocessing, training, testing, and validation of the data were conducted using PyTorch version 2.2.2 in Jupyter notebooks. The preprocessing step converted the images to RGB format and applied random horizontal and vertical transformations to ensure model robustness. These transformations simulate variations in orientation and perspective, improving the model's ability to generalize to real-world scenarios. The preprocessed data were then randomly split into 3 sets: 70% for training, 15% for testing, and 15% for validation.

The CNN model processes the input through convolution layers, which detect features such as edges and patterns using filters. Each subsequent layer captures increasingly complex details, with the first layer using 32 filters, followed by 64 in the second, 128 in the third, and 256 in the fourth. After each convolution, pooling layers are applied to down-sample the spatial dimensions of the feature maps using max pooling with a 2 × 2 kernel size, a stride of 1, and padding of 1. This reduces the computational load and helps the model generalize better. After pooling, the data are flattened, transforming the multi-dimensional feature maps into a 1-dimensional vector. This vector is then passed through fully connected layers, which progressively condense and simplify the features into 2 final digital outputs: stone (1) or no stone (0). In this study, a probability of greater than or equal to .5 was considered a stone and a probability less than .5 was not considered a stone.

The model was trained for 70 epochs, with an early stopping mechanism that halts training when there is little improvement in the outputs from the validation dataset. A confusion matrix and area-under-the curve (AUC) were used to evaluate the performance of both the testing and validation sets. Library (pROC) in the R-program 4.1.2 was used to calculate AUC. The weights and biases of the CNN model were exported as binary files for use in building a compiled application (ie, the CNN_images module).

Monitoring Stone Fragmentation During SWL

Two processes are involved: selecting the stone to be fragmented and monitoring the stone fragmentation during SWL.

Selecting the Stone. A program called "select_stone" identifies the stone of interest in the initial 640 × 480 image. The program provides real-time stone probabilities through the CNN_images module, which was integrated into the software (Fig. 1). Once the stone is marked, the probability is displayed on the screen, and the 50 × 50 image of the boxed stone is stored in a folder for comparison with other boxed images.

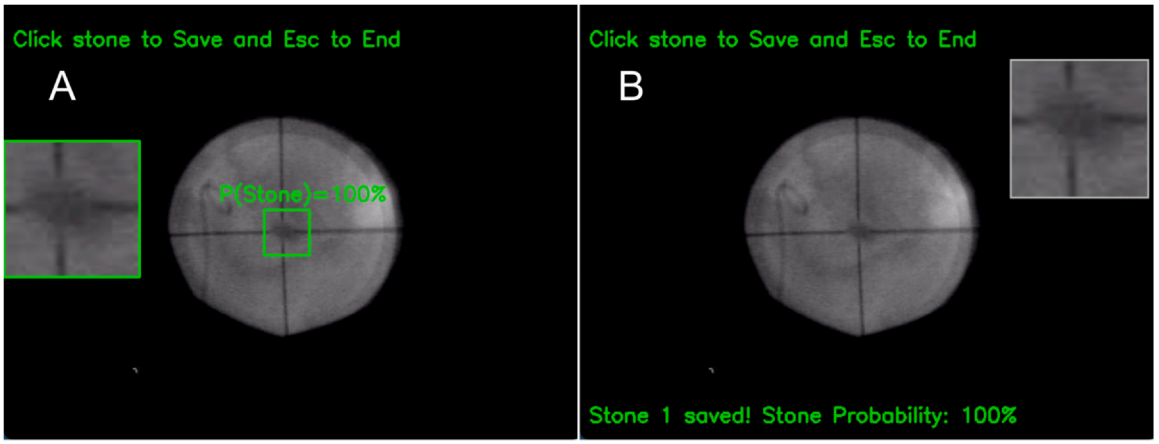

Figure 1. Screenshots of the select_stone application used to extract a PNG image of the stone. **(A)** A magnified green box highlights the stone, with the hovering stone probability displayed. **(B)** The top-right inset shows the saved image Stone_1.png, with a stone probability of 100%. The saved Stone_1.png will serve as a template for comparing stone images after each shockwave application.

Monitoring Stone Fragmentation. The find_stone application compares the initial box stone image (eg, Stone_1.png) to box images of the same size within the larger image representing the C-arm X-ray. Scanning is performed within the region of interest and progresses 1 pixel at a time across and down the current image (Supplementary Fig. 3). The box image with the highest R^2 value for the match is retained, and the probability match is a stone calculated by the CNN_image module.

The R^2 value for matching the initial boxed stone image to a subsequent boxed image is determined using OpenCV's template matching function, CV_TM_CCOEFF_NORMED, which computes the normalized cross-correlation coefficient. This coefficient is normalized to ensure the results are not affected by lighting conditions or pixel intensity variations, making the method more robust to changes in brightness or contrast between the template and the image. Coefficient values range from −1 to 1, with higher values indicating a better match. The results are squared, and the highest value is retained as the R^2 value for the match, which represents the percentage variability explained by the match.

Stone area of the best match is estimated by multiplying the initial stone area by the R^2 value of the match. The initial stone area is determined by the height and width of the original stone and the shape of the stone assumed to be elliptical using the formula:

$$\text{Stone area} = (\text{width}/2) \times (\text{height}/2) \times 3.14.$$

For example, a stone with a width = 8 mm and height = 12 mm would have an initial area of (8/2) × (12/2) × 3.14 = 75.4 mm^2. The stone area of the fragmented stone was determined by the initial stone area multiplied by the R^2 of the match between the initial stone and the fragmented stone. If R^2 = 0.57 (which represents a 43% stone loss) for the match between the initial stone and the fragmented stone, the fragmented stone would have an area of 75.4 × 0.57 = 42.8 mm^2.

Arbitrary thresholds were set for the percentage of stone loss and stone probability. If the percentage of stone loss exceeded 75%, meaning the normalized cross-correlation coefficient of the match was < ± 0.5 or the stone probability was < .5, the stone was reported as not found.

A signal notification system was developed using the relationship between the area of the initial stone images and the smallest area of the stone image (representing the largest stone loss) attained during the shockwave treatment with a runtime of about a second.

RESULTS

Stone Probability Calculator

After 52 of the 70 possible training epochs, a regularization technique was triggered to early stop, thus preventing over-fitting and improving model performance. Supplementary Figure 4 shows the convergence of the training and validation datasets over the epochs. The confusion matrices revealed overall accuracies of 0.96 for the validation dataset and 0.94 for the test dataset (Supplementary Tables). AUC analyses revealed overall scores of 99.2% for the validation dataset and 98.7% for the test dataset (Supplementary Fig. 5). These results are consistent with the concept that the outputs can accurately predict whether an image contains a stone or not. The compiled application was called CNN_images and integrated as a module to subsequent programs. The runtime for the compiled module was less than 5 ms.

Model Development

Stone selection: To select a stone or stones in the C-arm image, the "select_stone" application was used. This application features a hovering box that displays stone

probabilities in real time (Fig. 1). The operator clicks the mouse to place a 50 × 50 green box around the stone with the highest probability. The selected image is then saved and automatically compared to all subsequent stone images generated during the shockwave treatment.

Signal Notification System. The signal notification system was developed based on the relationship between the area of the initial boxed stone images and the areas of boxed stone images captured during shockwave treatments from 522 patients. The initial stone sizes had an average area of 80.1 mm^2 with a standard deviation of 90.0 mm^2. Most stones were located in the kidneys (85%), with the remainder in the ureters (15%).

Data points representing the areas of initial boxed stone images produced a line of equality (Supplementary Fig. 6). The distribution of data shows that stones with larger initial areas are associated with greater variation in stone size during shockwave applications. This finding suggests that more shockwaves are required to fragment larger stones.

The predicted final stone area (represented by the red regression line) was determined based on the stone image with the highest percentage loss relative to the initial stone image during a treatment. The regression equation was: predicted final stone area = 0.45 × initial stone area + 1.65, with an R^2 value of 0.84. The R^2 value indicates that the equation accounts for 84% of the variability in the data.

A signal notification system was developed using the regression equation and the 90% confidence interval (CI) (Supplementary Fig. 7). The signal is green for stone areas smaller than the lower boundary of the CI, indicating it is safe for the operator to continue delivering shockwaves to the stone. The signal is yellow for stone areas greater than the lower boundary but smaller than the upper boundary of the CI, indicating the operator should proceed with caution in delivering shockwaves. The signal is red for stone areas greater than the upper boundary of the CI, indicating that the maximum stone area loss has been achieved and shockwaves should stop.

Testing the Signal Notification System

The notification system was tested on 251 treatment samples, yielding the following results: 86 treatments (34%) yielded green signals only (Supplementary Image Files 1), 73 treatments (29%) yielded green and yellow signals (Supplementary Image Files 2), 27 treatments (11%) yielded green and red signals (Supplementary Image Files 3), and 65 treatments (30%) yielded green to red colors (Supplementary Image Files 4). Treatments yielding only green signals suggest that the stone may not have been adequately fragmented and/or that the stone was too hard to break. Treatments yielding green to yellow signals indicate that the stone was fragmented to the predicted final stone area. Treatments with green and red signals (but not yellow) suggest that not all stone images were captured during the treatment. Treatments yielding green, yellow, and red signals suggest that the stone was fragmented beyond the predicted final stone area.

Figure 2 shows 6 images in sequential order for one treatment session. The 11 mm by 11 mm stone was located in the Ureteral Pelvic Junction. Panel A serves as a control, with 0% stone loss and stone probability of 1. The top-right inset shows the initial stone, while the lower-right inset shows the current stone within the green box in the middle of the larger image. Panel B shows the images after shockwave application, with 38.1% stone loss. Subtle differences can be observed between the top- and bottom-right inset images. The notification signal has shifted to yellow in Panels C-E display stone losses of 52.7%, 53.2%, and 56.0%, respectively. The notification signal in Panel F is red, indicating that to stop shockwave delivery as stone loss reaches 56.1%. Note that it is visually difficult to see the stone in the image but the stone probability = 1, indicating fragments are visible by the CNN.

Supplementary Figure 8 shows 6 images in sequential order for another treatment session. The 10 mm by 10 mm stone was located in the mid-Calyx. Panel A serves as a control, with 0% stone loss and a stone probability of 1. Panels B-D show the images after shockwave application, with stone losses of 34.8%, 35.2%, and 43.3%, respectively. In panel E, the signal notification system turns yellow as stone loss reaches 51.9%. Panel F shows the system turning red, signaling the operator to stop shockwave delivery as stone loss reaches 59.8%. Similar to Figure 2 panel F, the stone probability = 1 because the CNN_image module detects stone fragments.

Supplementary Figure 9 shows 6 images in sequential order for a third treatment session. The 9 mm by 9 mm stone was located in the upper Calyx. Panel A serves as a control, with 0% stone loss and a stone probability of 1. Panels B and C show images after shockwave application, with stone losses of 37.2% and 42.9%, respectively. Panels D and E show the notification system turning yellow as stone losses reach 51.9% and 54.5%, respectively. Panel F shows the system turning red, signaling the operator to stop shockwave delivery as stone loss reaches 59.1%.

The results of the signal notification system testing demonstrate its ability to accurately track and indicate the progression of stone fragmentation during treatment. The system successfully identified varying levels of stone loss, with distinct color signals corresponding to specific thresholds of R^2 of the match and stone probability.

The images from the treatment sessions (Fig. 2, Supplementary Figs. 8 and 9) further validated the functionality of the notification system that corresponded to observable changes in stone loss and fragmentation. As stone loss increased, the system transitioned from green to yellow, indicating caution, and ultimately to red, signaling the need to stop

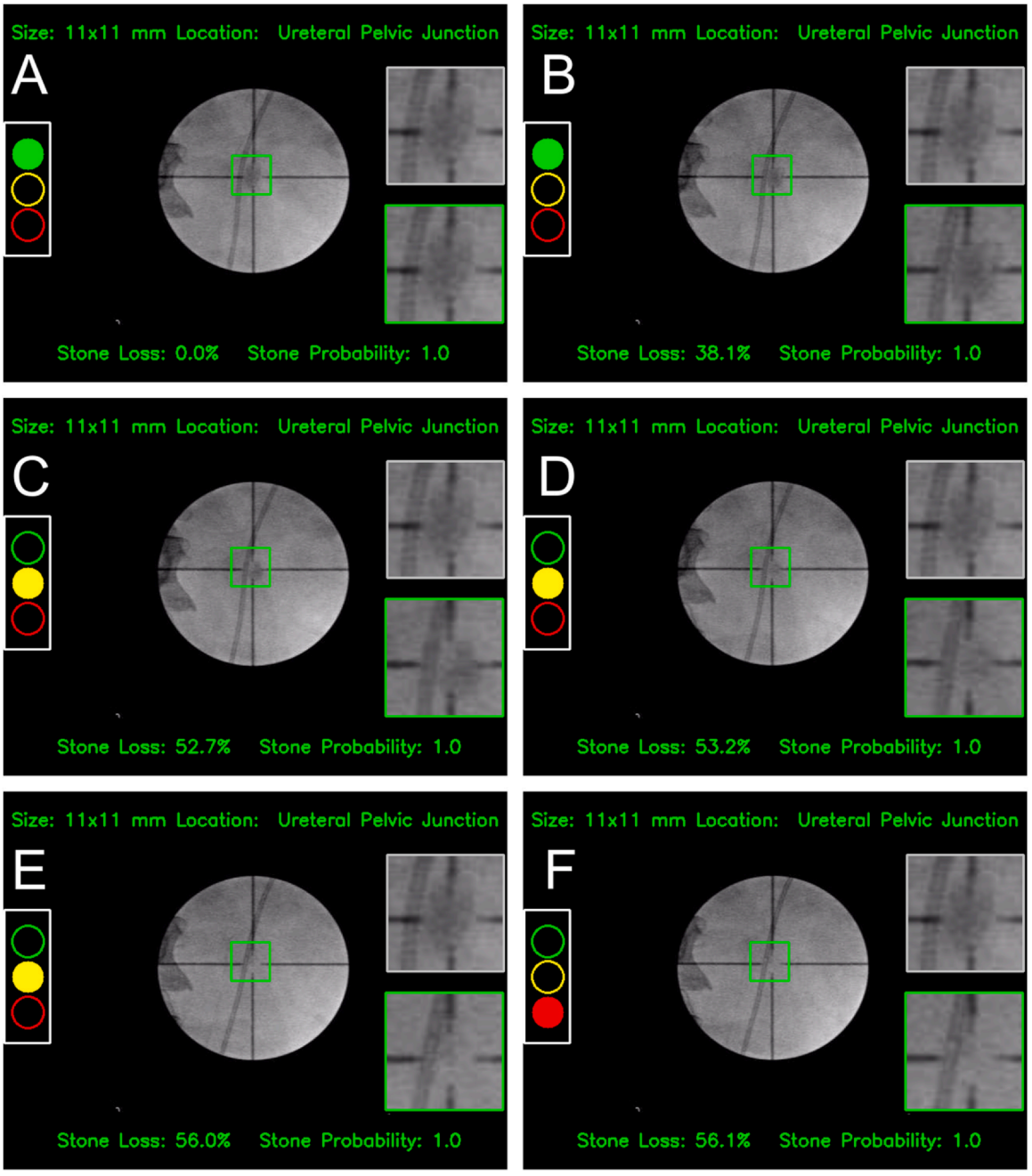

Figure 2. Composite of sample 4_52 showing stone fragmentation. The top-right image shows the original boxed stone for comparison, while the lower-right images display the current boxed stone. Stone loss progressively increases from Panels **(A)-(F)**. Panels **(A)** and **(B)** depict fragmentation with a green signal. Panels **(C)-(E)** depict a yellow cautionary signal. Panel **(F)** depicts a red signal, indicating that shockwaves should stop.

shockwave delivery to prevent possible complications. These findings underscore the potential of the notification system to enhance treatment precision, offering valuable guidance for operators to optimize stone fragmentation and minimize complication risks.

DISCUSSION

Various techniques have been used to quantify urinary stones, each with unique strengths and limitations. High-resolution computed tomography[22,23] and kidney-ureter-bladder X-rays[24] effectively estimate the stone area before SWL but are impractical for real-time monitoring during treatment. Ultrasound imaging provides continuous monitoring and is effective for detecting radiolucent stones[25]; however, its resolution can be limited and highly operator-dependent.[26] Fluoroscopy, which generates real-time C-arm X-ray images, enables visualization of stones during SWL but exposes patients to ionizing radiation and has limited sensitivity for detecting radiolucent stones.[6]

Fluoroscopy was used in this study because it represents the most feasible option for developing real-time metrics to assess stone fragmentation during SWL. This approach is not applicable to computed tomography scans, which are not collected in real time, nor to ultrasound imaging, due to unavailable data for testing.

Visual observation alone does not sufficiently convey shockwaves impact on the stone. For example, an operator cannot accurately determine how much a stone has been fragmented after a specific application of shockwaves solely by visually comparing the first image to the current image. The new metric helps operators evaluate the effectiveness of shockwaves on the stone and establishes a foundation for AI-guided, automated SWL systems capable of operating in remote settings (see Future Innovations). To our knowledge, this is the first study to propose a metric for measuring changes in stone area during treatment and a signal notification system to support operators during SWL sessions.

The 2-pronged approach combines the R^2 value of the match between the initial boxed image and the current box and stone probability. The R^2 value of the match is used to locate the stone of interest within the larger image and provide information on SWL effectiveness in terms of stone fragmentation (ie, stone loss). The CNN_image module determines whether the boxed image contains a stone. Notably, this module operates independently of the R^2 match and provides information on the presence of a stone regardless of whether it is whole or fragmented. That is, even if the stone is fragmented into tiny grains, the stone probability could still exceed .5. Combining the R^2 value of the match with the stone probability significantly enhances accuracy, as demonstrated by the examples in this study.

The signal notification system, based on the distribution around the regression line representing the smallest stone areas relative to the initial stone areas, provides a generalizable guideline for operators. This system could be further enhanced by incorporating data from thousands of ongoing SWL treatments using the programs developed in this study.

Strengths and Limitations

The strength of this study lies in its broad applicability: the models were based on treatments conducted across multiple institutions by various medical professionals using different SWL instruments, ensuring the results are generalizable beyond a single institution, professional, or instrument. Since all SWL treatments in this study were conducted in adherence to the guidelines set by the American Urological Association and European Association of Urology, the new metrics are inherently aligned with these established standards.

One limitation of this study is its retrospective design, which may have introduced biases and reduced the predictive accuracy of the models. For example, the lack of time stamps on SWL session images made it challenging to determine the exact sequence of events. The order of images was inferred through visual inspection, potentially introducing human error. Incorporating time stamps for each image captured after a shockwave application would significantly enhance the accuracy and reliability of the models.

Another limitation stems from the possibility that operators did not consistently include all images from a treatment session in the data provided. This selective image capture could omit crucial data points, potentially skewing the model's predictions. An automated system for recording images after each SWL application would not only standardize data collection but also improve the robustness and predictive power of the models. Prospective studies could address these limitations and enhance the findings further.

Of note, the R^2 value derived from the normalized cross-correlation coefficient accounts for changes in the stone's orientation caused by patient movement or shockwave-induced shifts. While this method does not account for changes outside the 2-dimensional imaging plane or the green box, multiplying the R^2 value by the initial stone area serves as a proxy for the current stone size. Although this proxy offers valuable insights, it may not fully reflect the actual stone size due to the resolution limitations of C-arm X-rays in capturing fine fragmentation details.

While this study focused on fluoroscopic imaging, applying the same methodology to ultrasound images could offer significant advantages, including lower radiation exposure and improved detection of radiolucent stones. However, feasibility depends on the availability of consistent, high-resolution ultrasound data during SWL, which I am actively investigating for future work.

Future Innovations

Real-time monitoring of stone status during shockwave treatment is crucial for developing a semi-automated, computer-assisted SWL system. By integrating stone status with key shockwave parameters—such as power level, shock rate, and shock counts—AI-driven systems could optimize shockwave applications in real time. A previous study predicting future shockwave parameters from past data[21] lacked this critical input, with stone status serving as the missing link to fully enable this advanced approach.

The need for such innovation is underscored by the rising global incidence and prevalence of kidney stones, likely driven by dietary practices and climate change.[27] In the United States alone, approximately 11% of the population will experience kidney stones during their lifetime.[28] Developing a semi-automated and standardized SWL approach will be essential for addressing this growing burden, particularly in challenging environments such as remote settings (eg, arid deserts) and space exploration. Specifically, extended spaceflight results in a urinary environment saturated with stone-forming salts, increasing the risk of stone formation.[29,30] In such scenarios, where access to highly trained urologists is

limited, a technician- and AI-guided system could autonomously perform SWL, reducing treatment complications and costs. This approach would ensure effective urinary stone management under extreme conditions, safeguarding both health and mission success.

Ethics Declaration

This research relied on the analysis of anonymized X-ray data obtained through the International Kidney Stone Registry. The dataset contained no identifiable information, ensuring full data privacy. No patient-identifiable records were used at any point. Further details about the dataset are available at the Kidney Stone Registry: http://kidneystoneregistry.com.s3-website-us-west-2.amazonaws.com/. At the time of analysis, all data were fully anonymized and de-identified. No personal identifiers were accessible to the research team. This study was conducted as a retrospective analysis of anonymized records, in accordance with standard ethical guidelines for the secondary use of clinical data.

Disclosures

This research did not receive any specific grant from funding agencies in the public, commercial, or not-for-profit sectors.

CRediT Authorship Contribution Statement

Peter A. Noble: Writing – review & editing, Writing – original draft, Visualization, Validation, Supervision, Software, Resources, Project administration, Methodology, Investigation, Formal analysis, Data curation, Conceptualization.

Declaration of Competing Interest

The author declares that he has no known competing financial interests or personal relationships that could have appeared to influence the work reported in this paper.

Declaration of Generative AI and AI-Assisted Technologies in the Writing Process

During the preparation of this work, the author used ChatGPT to proofread the manuscript. After using this tool/service, the author reviewed and edited the content as needed and takes full responsibility for the content of the publication.

Acknowledgment

The author thanks Dr Alex Pozhitkov from the City of Hope Cancer Research Center for his critical comments in an earlier version of the manuscript.

Appendix A. Supporting information

Supplementary data associated with this article can be found in the online version at doi:10.1016/j.urology.2025.07.044.

References

1. Chaussy C, Brendel W, Schmiedt E. Extracorporeally induced destruction of kidney stones by shock waves. *Lancet*. 1980;2:1265–1268. https://doi.org/10.1016/s0140-6736(80)92335-1
2. McAteer JA, Evan AP. The acute and long-term adverse effects of shock wave lithotripsy. *Semin Nephrol*. 2008;28:200–213. https://doi.org/10.1016/j.semnephrol.2008.01.003
3. Wang J-C, Zhou Y. Quantitative evaluation of stone fragments in extracorporeal shock wave lithotripsy using a time reversal operator. *AIP Conf Proc*. 2017;1821:150004. https://doi.org/10.1063/1.4977648
4. Lingeman JE, Matlaga BR, Evan AP. Surgical management of upper urinary tract calculi. In: Wein AJ, Kavoussi LR, Novick AC, eds. *Campbell's Urology*. 9th ed. Saunders Elsevier; 2007:1431–1507.
5. Schmitt RM, Wurster H, Kraus W, Bibinger M. The effects of errors in positioning lithotriptor and imaging kidney stones ultrasound. Proceeding of the 12th Annual International Conference of the IEEE Engineering in Medicine and Biology Society; 1990. doi:10.119/IEMBS.1990.691064.
6. Leighton TG, Fedele F, Coleman AJ, et al. A passive acoustic device for real-time monitoring of the efficacy of shockwave lithotripsy treatment. *Ultrasound Med Biol*. 2008;34:1651–1665. https://doi.org/10.1016/j.ultrasmedbio.2008.03.011
7. Noble PA, Hamilton BD, Gerber G. Stone decision engine accurately predicts stone removal and treatment complications for shock wave lithotripsy and laser ureterorenoscopy patients. *PLoS One*. 2024;19:e0301812. https://doi.org/10.1371/journal.pone.0301812
8. Noble PA. A smart computer program to assist healthcare providers in selecting the best treatment for patients with urinary stones. *Adv J Urol Nephrol*. 2024;6:01–05.
9. Estrade V, Daudon M, Richard E, et al. Deep morphological recognition of kidney stones using intra-operative endoscopic digital videos. *Phys Med Biol*. 2022;67. https://doi.org/10.1088/1361-6560/ac8592
10. Kim YI, Song SH, Park J, Youn HJ, Kweon J, Park HK. Deep-learning segmentation of urinary stones in noncontrast computed tomography. *J Endourol*. 2023;37:595–606. https://doi.org/10.1089/end.2022.0722
11. Huang ZH, Liu YY, Wu WJ, Huang KW. Design and validation of a deep learning model for renal stone detection and segmentation on kidney-ureter-bladder images. *Bioengineering (Basel)*. 2023;10:970. https://doi.org/10.3390/bioengineering10080970
12. Cellina M, Cè M, Rossini N, et al. Computed tomography urography: state of the art and beyond. *Tomography*. 2023;9:909–930. https://doi.org/10.3390/tomography9030075
13. Choi HS, Kim JS, Whangbo TK, Eun SJ. Improved detection of urolithiasis using high-resolution computed tomography images by a vision transformer model. *Int Neurourol J*. 2023;27(suppl 2):S99–S103. https://doi.org/10.5213/inj.2346292.146
14. Asif S, Zhao M, Chen X, Zhu Y. StoneNet: an efficient lightweight model based on depthwise separable convolutions for kidney stone detection from CT images. *Interdiscip Sci*. 2023;15:633–652. https://doi.org/10.1007/s12539-023-00578-8
15. Caglayan A, Horsanali MO, Kocadurdu K, Ismailoglu E, Guneyli S. Deep learning model-assisted detection of kidney stones on computed tomography. *Int Braz J Urol*. 2022;48:830–839. https://doi.org/10.1590/S1677-5538.IBJU.2022.0132
16. Alves BM, Belkovsky M, Passerotti CC, Artifon ELA, Otoch JP, Cruz JASD. Use of artificial intelligence for sepsis risk prediction after flexible ureteroscopy: a systematic review. *Rev Col Bras Cir*. 2023;50:e20233561. https://doi.org/10.1590/0100-6991e-20233561-en

17. Hong X, Liu G, Chi Z, Yang T, Zhang Y. Predictive model for urosepsis in patients with Upper Urinary Tract Calculi based on ultrasonography and urinalysis using artificial intelligence learning. *Int Braz J Urol*. 2023;49:221–232. https://doi.org/10.1590/S1677-5538.IBJU.2022.0450
18. Nakamae Y, Deguchi R, Nemoto M, et al. AI prediction of extracorporeal shock wave lithotripsy outcomes for ureteral stones by machine learning-based analysis with a variety of stone and patient characteristics. *Urolithiasis*. 2023;52:9. https://doi.org/10.1007/s00240-023-01506-7
19. Rice P, Pugh M, Geraghty R, Hameed BZ, Shah M, Somani BK. Machine learning models for predicting stone-free status after shockwave lithotripsy: a systematic review and meta-analysis. *Urology*. 2021;156:16–22. https://doi.org/10.1016/j.urology.2021.04.006
20. Hameed BMZ, Shah M, Naik N, Singh Khanuja H, Paul R, Somani BK. Application of artificial intelligence-based classifiers to predict the outcome measures and stone-free status following percutaneous nephrolithotomy for staghorn calculi: cross-validation of data and estimation of accuracy. *J Endourol*. 2021;35:1307–1313. https://doi.org/10.1089/end.2020.1136
21. Chen Z, Zeng DD, Seltzer RGN, Hamilton BD. Automated generation of personalized shock wave lithotripsy protocols: treatment planning using deep learning. *JMIR Med Inform*. 2021;9:e24721. https://doi.org/10.2196/24721
22. Abdelhamid M, Mosharafa AA, Ibrahim H, et al. A prospective evaluation of high-resolution CT parameters in predicting extracorporeal shockwave lithotripsy success for upper urinary tract calculi. *J Endourol*. 2016;30:1227–1232. https://doi.org/10.1089/end.2016.0364
23. Cui HW, Silva MD, Mills AW, North BV, Turney BW. Predicting shockwave lithotripsy outcome for urolithiasis using clinical and stone computed tomography texture analysis variables. *Sci Rep*. 2019;9:14674. https://doi.org/10.1038/s41598-019-51026-x
24. Choi SL, Park SB, Yang S, et al. Detection of ureteral stones in kidney ureter bladder radiography: usefulness of digital post-processing. *Curr Med Imaging*. 2021;17:1356–1362. https://doi.org/10.2174/1573405617666210218094812
25. Karlin G, Marino C, Badlani G, Smith AD. Benefits of an ultrasound-guided ESWL unit. *Arch Esp Urol*. 1990;43:579–581.
26. Wieczorek AP, Woźniak MM, Tyloch JF. Errors in the ultrasound diagnosis of the kidneys, ureters and urinary bladder. *J Ultrason*. 2013;13:308–318. https://doi.org/10.15557/JoU.2013.0031
27. Romero V, Akpinar H, Assimos DG. Kidney stones: a global picture of prevalence, incidence, and associated risk factors. *Rev Urol*. 2010;12:e86–e96.
28. Scales Jr CD, Smith AC, Hanley JM, Saigal CS. Urologic Diseases in America Project. Prevalence of kidney stones in the United States. *Eur Urol*. 2012;62:160–165. https://doi.org/10.1016/j.eururo.2012.03.052
29. Whitson PA, Pietrzyk RA, Sams CF. Space flight and the risk of renal stones. *J Gravit Physiol*. 1999;6:P87–P88.
30. Patel SR, Witthaus MW, Erturk ES, Rabinowitz R, Nakada SY. A history of urolithiasis risk in space. *Can J Urol*. 2020;27:10233–10237.